Synthesis of CeO_2/rGO Nanocomposites by Laser Ablation in Liquid Method and the Characterization for Advanced Materials Development

Mengqi Shi, Yoshitaka Kitamoto, and Hiroyuki Wada*

Tokyo Institute of Technology, Japan
**Corresponding author's e-mail: wada.h.ac@m.titech.ac.jp*

This research investigates the synthesis and characterization of CeO_2-rGO (cerium oxide-reduced graphene oxide) composites for potential applications. CeO_2 nanoparticles were synthesized using the laser ablation in liquid method (LAL), resulting in well-dispersed, spherical nanoparticles with a narrow size distribution. The composites were fabricated by decorating the CeO_2 nanoparticles onto the surface of reduced graphene oxide (rGO) sheets. The structural and morphological properties of the composites were analyzed using techniques such as scanning electron microscopy (SEM), X-ray diffraction (XRD), and energy-dispersive X-ray spectroscopy (EDS). The results demonstrated the successful combination of CeO_2 nanoparticles with rGO, with CeO_2 nanoparticles stably adsorbed on the rGO sheets. The UV-vis spectra and Tauc plots revealed changes in the absorption peak and band gap, indicating the incorporation of CeO_2 into the rGO structure. The changing of the energy band gap of the CeO_2-rGO composites was attributed to the synergistic effect between rGO and CeO_2, improving charge transfer. The research highlights the potential of CeO_2-rGO composites for applications requiring enhanced electrical properties, opening up possibilities in various fields.
DOI: 10.2961/jlmn.2023.03.2010
Keywords: CeO_2 nanoparticle, CeO_2-rGO composites, laser ablation in liquid method, synergistic effect

1. Introduction

The laser ablation in liquid (LAL) method, a versatile and promising approach, has garnered attention as an alternative to conventional methods for synthesizing nanomaterials with tailored properties. Traditionally, the precipitation method has been widely employed for synthesizing nanomaterials in small sizes [1]. However, this method often leads to uncontrollable particle size distribution and poor dispersibility [2], negatively impacting the performance of electrodes designed for various applications. Consequently, laser ablation in liquid (LAL) method is considered an alternative process. This physical method has gained attention due to its ability to overcome the limitations of traditional precipitation techniques. LAL is a versatile technique that enables the synthesis and fabrication of various nanostructures by subjecting a target material to laser irradiation in a liquid medium [3, 4]. This method offers several advantages, including precise control over nanoparticle size [5,6], morphology [7], and dispersity [8]. and notably, high purity, as it allows the synthesis of nanoparticles without the need for additional organic surfactants or similar additives [6]. The control of the smaller nanoparticle size that can be achieved due to the laser fragmentation process in the liquid in a specific LAL process [9, 10, 11, 12] has great potential in enhancing the performance of CeO_2/rGO nanocomposite for various applications. Smaller particles generally exhibit greater surface area, which can improve catalytic activity and electric properties.

In recent years, graphene oxide (GO) has emerged as a promising material for drug delivery, capacitors, and electric coatings [13, 14, 15]. GO possesses excellent chemical stability [16], a large surface area [16, 17], and a tunable electrode dimension [18], making it an ideal candidate of electric coating for electronic devices. However, the pristine form of GO typically exhibits lower electrical properties due to the presence of oxygen functional groups [19, 20]. This can limit its lower detection limit and response time for the analysis of interest. The reduced graphene oxide (rGO) outperforms graphene oxide (GO) in electrochemical applications due to reduced oxygen functional groups and restored π-conjugation [21]. rGO offers enhanced electrochemical activity with more active sites, making it ideal for electrodes in supercapacitors [22], batteries [23], fuel cells [24], and especially sensors [25]. Its higher specific surface area leads to increased capacitance, improved ion diffusion, and better analyte adsorption.

The preparation of rGO from GO such as the chemical [26, 27] or thermal reduction [27], typically involves harsh chemical treatments, such as the use of strong reducing agents [28] or high-temperature annealing [29]. These processes may introduce impurities or damage the graphene structure, compromising the electrical performance. In contrast, the ultrasonication method offers a milder approach to peel rGO from GO by utilizing ultrasonic energy to break weak intermolecular forces [30]. This method provides a simpler and more efficient means of obtaining rGO with improved electrical properties, without the need for harsh chemical treatments.

Furthermore, the combination of additional functional materials can further improve the electrical performance of GO-based material, which is underpinned by the formation of a p-n junction between these materials. [31]. This junction

creates a unique interface where the electron-rich properties of rGO meet the electron-deficient characteristics of CeO_2. As a result, an efficient charge transfer mechanism is established, facilitating the rapid migration of charge carriers and promoting gas molecule interactions with the electrode surface [32, 33] in the application of sensors. Besides, cerium dioxide (CeO_2) is widely recognized for its exceptional catalytic properties and high selectivity towards specific gases [34, 35], leveraging high selectivity compared to the individual components alone.

In this study, a comparison of the precipitation method and LAL method of CeO_2 manufacturing was made to verify a suitable process that manufactures CeO_2 more beneficial to combining with rGO. The LAL method exhibited notable advantages in the production of CeO_2 nanoparticles with a homogeneous size distribution below 50 nm and a spherical morphology, highlighting the efficacy of this physical synthesis approach for CeO_2 fabrication. In addition, the utilization of the ultrasonication method provides advantages in terms of rGO preparation in this study. More importantly, this work demonstrated a changing energy band gap of the CeO_2-rGO composites achieved by harnessing the synergistic effects derived from their combined properties.

2. Experimental

2.1 Preparation of CeO_2 nanoparticle

Laser ablation in liquid method:

Micron-sized CeO_2 powder (Kanto Chemical Co., INC., 99.99%) was compacted into 0.3 mm tablets at 150 MPa. The tablets were then sintered at 1250 ℃ for 2 h to create a CeO_2 irradiation target bulk. The target was placed at the center of the bottom of a glass bottle and covered with 20 mL of pure water. An Nd: YAG laser operating at a wavelength of 532 nm with a second harmonic generation of 10 Hz was used for laser ablation. The laser settings were as follows: Maximum output power of approximately 3.6 W, energy of 360 mJ/pulse, and pulse width of 13 ns. The laser beam was split by a polarizing beam splitter (PBS), adjusted by a half-wave plate (HWP), refracted 90° through a plane mirror, and collected by a condenser. The CeO_2 nanoparticle suspension liquid was prepared by subjecting the target to a 5 J/cm^2 laser beam for 30 mins.

Precipitation method:

A precursor solution was prepared by dissolving 4.35 g of $Ce(NO)_3 \cdot 6H_2O$ (SIGMA-ALDRICH, Co., 99.99%) in 50 mL of deionized water. Then, 3 mL of ammonia was added drop by drop, and the mixture was stirred for 24 hours. The solution initially had a light brown color, which changed to light yellow after 10 hours, indicating the transition of Ce^{3+} to Ce^{4+} [36]. After centrifugation (3000 rpm, 20 min), the precipitate was obtained. The precipitate was washed several times with DI water and ethanol, then dried overnight. The dried precipitate was sintered at 900 ℃ for 2 hours to remove impurities and obtain CeO_2 nanoparticles.

2.2 Preparation of CeO_2-rGO Nanocomposite

Initially, 8 mg of reduced GO (SIGMA-ALDRICH, Co., 15-20 sheets, 10% edge-oxidized) was dispersed in 50 mL of pure water through 2 hours of ultrasonication to form an rGO suspension. CeO_2 nanoparticles prepared using the laser ablation method were added to the suspension in different mole ratios for each sample: rGO: CeO_2 ratios of 2:1, 1:1, and 1:2. After 30 minutes of ultrasonication and stirring under a PH value of 7.4, the suspension was left undisturbed for 24 hours to allow precipitation. The precipitate was then obtained through centrifugation and freeze-drying, resulting in successfully prepared CeO_2-rGO samples for each ratio.

2.3 Characterization

In this research, X-ray diffraction (XRD) was employed to identify each sample. Scanning electron microscopy (SEM) and dynamic light scattering (DLS) were used to characterize the morphology and size distribution of the nanoparticles and investigate their aggregation. Energy-dispersive X-ray spectroscopy (EDS) was utilized to examine the element distribution of the composites, while UV-vis spectroscopy was employed for quantitative analysis and calculation of the energy band gap.

3. Results and discussions

Figures 1 (a) and (b) illustrate the SEM images of CeO_2 nanoparticles synthesized by the precipitation and LAL methods, respectively. Figure 1 (c) presents the primary size distribution obtained from the two methods. The SEM image of the precipitation method (Figure 1 (a)) reveals CeO_2 nanoparticles with an average size of 83.4 nm, exhibiting an irregular, bulk, or polyhedral shape. Moreover, the precipitation method demonstrates a higher degree of size dispersity, with a wider range of particle sizes observed. In contrast, the SEM image of the LAL method (Figure 1 (b)) displays CeO_2 nanoparticles with an average size of 43.2 nm, exhibiting a remarkable uniformity in size and spherical shape. The nanoparticles synthesized via the LAL method exhibit a narrow size distribution and a significantly reduced presence of larger aggregate. The formation of spherical CeO_2 nanoparticles in the LAL method can be attributed to the unique process involved. In the laser ablation process, a laser pulse with high energy is focused on the cerium oxide bulk target submerged in the liquid medium (DI water) [37]. The intense laser energy causes localized heating and vaporization of the target material, resulting in the generation of a high-temperature, high-pressure plasma plume [38]. As the plasma plume rapidly expands and cools upon contact with the surrounding liquid, the supersaturated vapor undergoes rapid nucleation and condensation. The rapid cooling and condensation process promotes the formation of individual spherical nanoparticles [40, 41]. In the absence of any external perturbation, the LAL method lacks growth mechanisms that favor anisotropic particle growth [42], such as in the precipitation method [43], which makes CeO_2 nanoparticles much easier to form a spherical shape in pure water. In addition, the quenching effect [44], induced by the rapid heat transfer from the plasma plume to the liquid medium, prevents significant particle aggregation and facilitates the preservation of the spherical morphology.

The comparison of the secondary particle size distributions of the CeO_2 suspension liquids synthesized through the precipitation and LAL methods is shown in the DLS distribution (Figure 2). The laser ablation in liquid method shows a narrow distribution peak ranging from 20 to 100 nm, approximately. In contrast, the precipitation method exhibits a

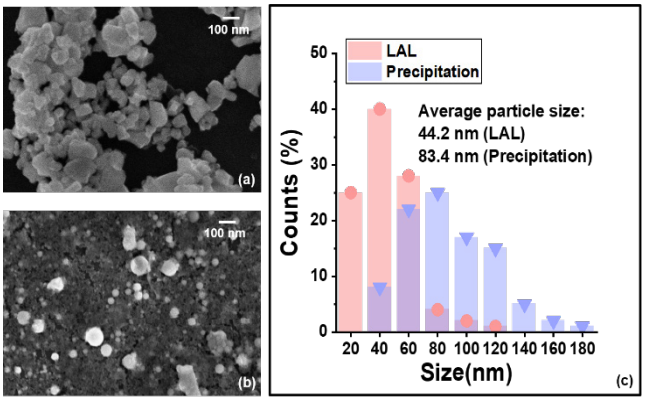

Fig. 1 SEM images of (a) raw material and nanoparticles at each fluence ((b) 75 mJ/cm^2, (c) 150 mJ/cm^2 and (d) 300 mJ/cm^2).

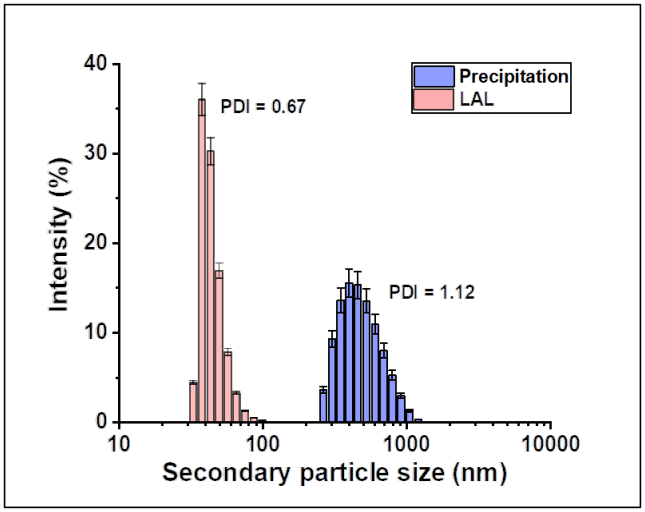

Fig. 2 DLS comparison secondary particle size distribution of CeO_2 suspension liquid made by precipitation method and laser ablation in liquid method.

Table 1 Calculation of the PDI value based on the secondary particle size distribution in Figure 2.

Method	Precipitation	LAL
M_w	558.1	32.8
M_n	497.1	48.6
PDI	1.12	0.67

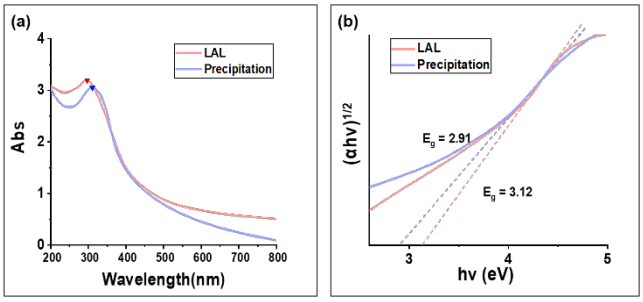

Fig. 3 (a) UV-vis of LAL and precipitation method. (b) Tauc plot of (a).

distribution peak spanning from 200 to 1000 nm, which is an order of magnitude larger than the primary particle size, signifying an obvious aggregation. In this research, to qualify the degree of size uniformity of a colloidal system, Table.1 presents the calculated PDI (polydispersity index) values for the secondary particle size distributions depicted in Figure 2, with lower values indicating a more monodisperse system [45]. The PDI was calculated by equation (1),

$$PDI = M_w / M_n \quad (1),$$

where M_w is the weight average molecular weight and M_n is the number average molecular weight. And equation (2) and (3) calculate M_w and M_n, respectively.

$$M_w = \Sigma M_i \times W_i / W_i \quad (2)$$
$$M_n = \Sigma M_i \times N_i / N_i \quad (3),$$

where W_i represents the weight fraction of particles with a specific molecular weight M_i, N_i represents the number fraction of particles with a specific molecular weight M_i, and M_i represents the molecular weight of particles in the distribution. The PDI value of the LAL method is calculated to be 0.67, in contrast, the precipitation method calculated a PDI of 1.12, signifying a polydisperse system with evident aggregation compare to the LAL method. These findings suggest that the LAL method yields CeO_2 particles with superior dispersion and reduced aggregation compared to the precipitation method. The spherical-shaped CeO_2 nanoparticles made by LAL method contribute to a reduction in aggregation. Spherical nanoparticles have a smaller surface area compared to irregular-shaped nanoparticles of the same volume, it minimizing the opportunities for particles to come into close contact and adhere to one another. And the smaller surface area can result in lower surface energy [46], making it less likely for spherical nanoparticles to aggregate. Additionally, the uniform surface charge distribution of spherical CeO_2 tends to be more stable in solution due to the repulsive forces between similarly positively charged particles (Figure. SI), which prevent aggregation and keep the particles dispersed in the solution.

Figure 3 (a) depicts the UV-vis spectra obtained for CeO_2 nanoparticles synthesized through the LAL and precipitation methods. Both curves show a strong UV absorption peak from 250 nm to 350 nm, approximately, which can be attributed to the electronic transitions between the oxygen 2p and cerium 4f bands in the CeO_2. A noticeable blue shift is observed in the absorption peak of the LAL method compared to the precipitation method. To further investigate the optical properties and determine the band gaps, a Tauc plot in Figure.3 (b) demonstrates a higher band gap for LAL-synthesized CeO_2 nanoparticles (3.12 eV) than the precipitation-synthesized sample (2.91 eV). Recording to the quantum size effect [47], this blue shift phenomenon indicates an increase of nanoparticles under 20 nm and a decrease in average nanoparticle size in the LAL [48].

Therefore, CeO_2 nanoparticles synthesized through LAL are smaller, spherical, and have a uniform size distribution serving as the ideal raw material to facilitate effective combination with GO in CeO_2/rGO complex fabrication.

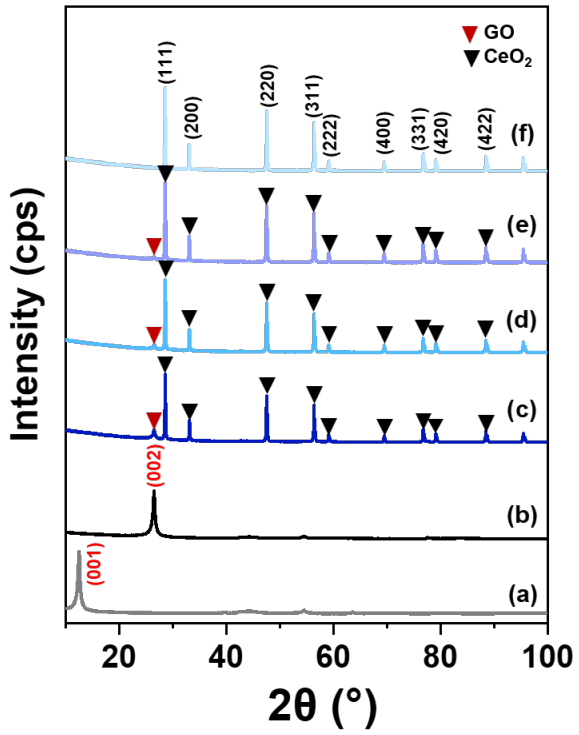

Fig. 4 XRD pattern of (a) GO (b) rGO (c) $1CeO_2/2GO$ (d) $1CeO_2/1GO$ (e) $2CeO_2/1GO$ (f) CeO_2.

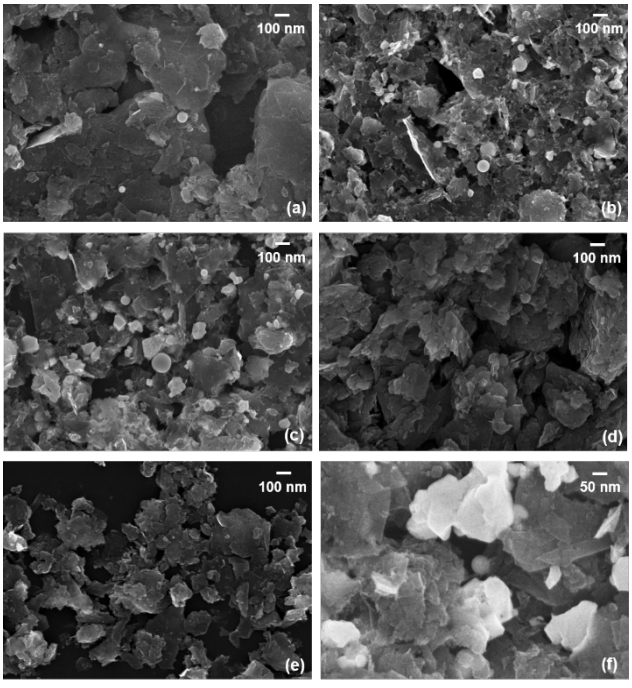

Fig. 5 SEM images of (a) $1CeO_2/2rGO$ (b) $1CeO_2/1rGO$ (c)$2CeO_2/1rGO$ (d) GO (e) rGO (f) $2CeO_2/1rGO$ in high magnification.

Table 2 Zeta potential of rGO and CeO_2.

Material	Zeta potential (ζ)
rGO	-42.4 ± 0.2
CeO_2	53.6 ± 2.1

The XRD patterns of raw GO, rGO, and CeO_2/rGO nanocomposites in different mole ratios, along with pure CeO_2, are shown in Figure 4. The GO peaks are marked in red, the presence of the (001) peak (Figure. 4(a)) in the raw GO spectrum indicates the presence of a well-stacked graphene oxide structure. However, the intensity of the (001) peak (Figure. 4(b)) disappeared in the rGO pattern and was replaced by the (002) peak after ultrasonication, indicating the successful exfoliation and reduction of GO into thin flakes of rGO. The intensity of XRD peaks decreased in rGO as the single-layer content of the carbon increased [49]. The CeO_2 peaks are marked with black inverted triangles at the (111), (200), (220), (311), (222), (400), (331), (420), and (422) crystallographic planes, indicating the presence of cubic fluorite structured CeO_2 in the samples (Figure. 4 (c-e)). Compared with CeO_2 nanoparticles (Figure4. (f)), CeO_2/rGO (Figure4. (c-e)) shows similar characteristic diffraction peaks, meanwhile, the rGO diffraction peaks almost disappeared with the increase of CeO_2 ratio. In the case of rGO, the reduction process of rGO by Ce^{3+} leads to the restoration of the conjugated sp2 carbon network, more compact structure, and decreased interlayer spacing making the XRD peak of rGO shifted to a higher angle [50]. More CeO_2 nanoparticles are evenly adsorbed between the rGO sheets, further reducing the interlayer spacing, and the attenuation effect of CeO_2 on X-rays is also the reason for the extreme decrease of the rGO diffraction peaks. The absence of any additional peaks in the XRD pattern suggests the absence of any significant second phases in the nanocomposites.

To study the combination situation of the complex, SEM images were obtained to investigate the morphology and structure in Figure 5. Comparative analysis of Figure 5 (d, e) revealed significant differences between GO and rGO. The sheet structure of rGO appeared thinner and smaller compared to GO, indicating the successful peeling off of graphene oxide layers during the ultrasonic process. This observation supports the findings of the diffraction peak changes observed in Figure 4, suggesting a structural transformation from GO to rGO. With the gradual increase in the proportion of CeO_2 (Figure.5 (a-c)), more pronounced adsorption of CeO_2 decorated between the gaps of rGO sheets. Spherical CeO_2 nanoparticles are stably adsorbed on the rGO sheets obviously in higher magnification (Figure 5 (f)), indicating an effective combination of CeO_2-rGO material. The opposite surface charges (Table. 2) of rGO and CeO_2 have exhibited an electrostatic effect in promoting the uniform adsorption and precipitation of the two materials during the standing process. At the same time, due to the combination of Ce^{3+} ions and oxygen-based functional groups, the cerium oxide nanoparticles are more stably embedded on the rGO surface, increasing charge mobility by the synergistic effect [51] between rGO and CeO_2 nanoparticles. However, at high concentrations of CeO_2, a slight agglomeration phenomenon was observed. During the ultrasonication process, it is important to note that high-intensity sound waves create localized regions of elevated temperature due to the phenomenon known as acoustic cavitation. In these regions, the rapid expansion and collapse of microbubbles generate intense heat [52], leading to localized heating of the surrounding liquid medium. This localized heating is high enough to promote

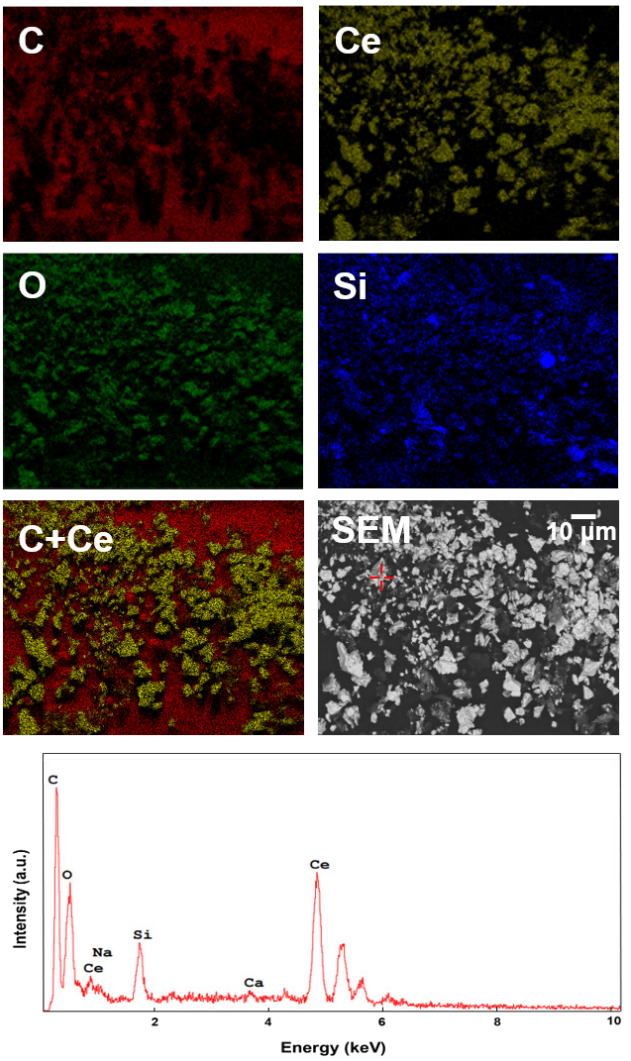

Fig. 6 SEM image and EDS mapping with enhanced contrast of the element distribution and uniformity analysis of the CeO_2-rGO complex in a molar ratio of 1:1.

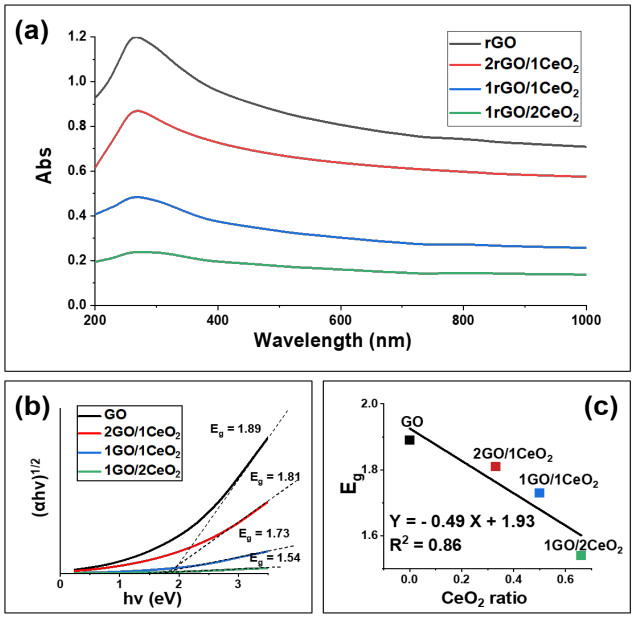

Fig. 7 (a) UV-vis of the effect on the complex ratio. (b) Tauc plot of (a). (c) Eg as a function of the CeO_2 ratio with the liner fitting.

the aggregation and melting of CeO_2 nanoparticles. The aggregation process is facilitated by the increased temperature, causing CeO_2 nanoparticles to come into close proximity and fuse together. Consequently, irregular-shaped aggregates and larger CeO_2 platelets are formed on the support material, which is consistent with the platelet-like structures observed in Figure. 5(f).

The EDS mapping was employed to investigate the elemental distribution and uniformity of a CeO_2-rGO nanocomposite with a molar ratio of 1:1. Figure 6 shows the SEM image of the CeO_2-rGO nanocomposite, and it serves as an example for conducting the EDS mapping analysis. The EDS mapping confirmed the presence of three elementary components: cerium (Ce), oxygen (O), and carbon (C). The mapping revealed that these elements were uniformly dispersed throughout the nanocomposite, which indicated a homogeneously decorating of CeO_2 nanoparticles on the surface of rGO. To assess the uniformity of the element distribution, several points were randomly selected for elemental analysis. Take one point aimed in red as an example, the elements intensity pattern demonstrated an even distribution of the elements, indicating a homogeneous dispersion.

Figure 7(a) presents the UV-vis spectra obtained for the CeO_2-rGO nanocomposites with varying mole ratios of CeO_2. The absorption peak is observed to decrease as the CeO_2 ratio increases. To further analyze the energy band gap of the nanocomposites, a Tauc plot (Figure. 7 (b)) was constructed based on the UV-vis spectra shown in Figure 7(a). The plot clearly demonstrates that the energy band gap gradually decreases proportionally with the increase in the amount of CeO_2. This phenomenon can be attributed to the synergistic effect between rGO and CeO_2 within the nanocomposites. rGO possesses exceptional electrical properties due to its two-dimensional hexagonal lattice structure and high charge carrier mobility [51]. By incorporating nanoparticles onto the graphene surface or within its layers, the conductive pathways can be further optimized. The CeO_2 nanoparticles can act as conductive bridges, improving the electron transfer between graphene nanosheets and enhancing overall electrical properties [53]. The incorporation of CeO_2 nanoparticles may introduce defects and surface states in the nanocomposites. These defects and surface states can contribute to the energy band structure and lead to a decrease in the energy band gap near the interface with rGO [54]. This enhancement in charge transfer can be beneficial for application in electrical components, where efficient charge transport is crucial for improved electrical performance.

4. Conclusion

In conclusion, this research compared CeO_2 nanoparticles synthesized through precipitation and laser ablation in liquid (LAL) methods. The precipitation method produced irregular-shaped nanoparticles with a wider size distribution, while the LAL method yielded smaller, spherical nanoparticles with a narrow size range and reduced aggregation. The LAL method's unique process promoted the formation of spherical nanoparticles. The LAL-synthesized nanoparticles also exhibited a blue shift in UV absorption and a higher band gap, indicating a smaller particle size. The CeO_2/rGO nanocomposites demonstrated effective combination and uniform dispersion of CeO_2 on rGO sheets, the synergistic effect between these two materials decreasing the energy

band gap. Overall, the LAL method offers advantages in producing well-dispersed, spherical CeO_2 nanoparticles for decorating rGO, leading to the development of CeO_2-rGO composites that exhibit enhanced electrical properties for application.

References

[1] H. C. Schwarzer and W. Peukert: Chem. Eng. Commun., 1191, (2004) 580.
[2] C. Nayral, E. Viala, P. Fau, F. Senocq, J. Jumas, A. Maisonnat, and B. Chaudret: Eur. J. Chem., 6, (2000) 4082.
[3] Z. Yan and D.B. Chrisey: J. Photochem. Photobiol., 13, (2012) 204.
[4] M. Hashida, H. Mishima, S. Tokita, and S. Sakabe: Opt. Express, 17, (2009) 15.
[5] V. Amendola and M. Meneghetti: Phys. Chem. Chem. Phys., 11, (2009) 3805.
[6] V. Amendola, D. Amans, Y. Ishikawa, N. Koshizaki, S. Scirè, G. Compagnini, and S. Reichenberger: Chem. Eur. J., 26, (2020) 9206.
[7] M.G. John and K.M. Tibbetts: Appl. Surf. Sci., 510, (2020) 145037.
[8] R.C. Forsythe, C.P. Cox, M.K. Wilsey, and A.M. Müller: Chem. Rev., 121, (2021) 7568.
[9] D. Zhang, Z. Li, and C. Liang: Sci. China Phys. Mech. Astron., 65, (2022) 274203.
[10] D. Zhang, B. Gökce, and S. Barcikowski: Chem. Rev., 117, (2017) 3990.
[11] D. Zhang, Z. Li, and K. Sugioka: J. Phys. Photonics, 3, (2021) 042002.
[12] D. Zhang, J. Liu, and C. Liang: Sci. China Phys. Mech. Astron., 60, (2017) 074201.
[13] J. Liu, L. Cui, and D. Losic: Acta Biomaterialia, 9, (2013) 9243.
[14] M.P. Down, S.J. Rowley-Neale, G.C. Smith, and C.E. Banks: ACS Appl. Energy Mater, 2, (2018) 707.
[15] T. Hibino, S. Kakimoto, and M. Sano: J. Electrochem. Soc., 146, (1999) 3361.
[16] M.M. Shahid, P. Rameshkumar, A. Pandikumar, H.N. Lim, Y.H. Ng, and N.M. Huang: J. Mater. Chem. A, 3, (2015) 14458.
[17] H. Beitollahi and F. G. Nejad: Electroanalysis, 28, (2016) 2237.
[18] S. Yang, B. Xu, J. Zhang, X. Huang, J. Ye, and C. Yu: J. Phys. Chem., 114, (2010) 4389.
[19] C.R. Minitha, V.S. Anithaa, V. Subramaniam, and R.T.R. Kumar: ACS Omega, 3, (2018) 4105.
[20] X. Wang, X. Li, Y. Zhao, Y. Chen, J. Yu, and J. Wang: RSC Adv., 6, (2016) 52339.
[21] D. Yuan, W. Huang, X. Chen, Z. Li, J. Ding, L. Wang, H. Wan, W. Dai, and G. Guan: Appl. Surf. Sci., 489, (2019) 658.
[22] R.K. Mishra, G.J. Choi, Y. Sohn, S.H. Lee, and J.S. Gwag: Chem. Commun., 56, (2020) 2893.
[23] C. Zhao, H. Gao, C. Chen, H. Wu, and J. Mater: Chem. A, 3, (2015) 18360.
[24] I.V. Pushkareva, A.S. Pushkarev, V.N. Kalinichenko, R.G. Chumakov, M.A. Soloviev, Y. Liang, P. Millet, and S.A. Grigoriev: Catalysts, 11, (2021) 256.
[25] L. Han, C.M. Liu, S.L. Dong, C.X. Du, X.Y. Zhang, L.H. Li, and Y. Wei: Biosens., 87, (2017) 466.
[26] M. Fathy, A. Gomaa, and F. A. Taher: J. Mater. Sci., 51, (2016) 5664.
[27] A. Ahmed, A. Singh, S. Young, V. Gupta, M. Singh, and S. Arya: Compos. Part A Appl., 165, (2023) 107373.
[28] T. Kuila, A.K. Mishra, P. Khanra, N.H. Kim, and J.H. Lee: Nanoscale, 5, (2013) 52.
[29] J.D. Renteria, S. Ramirez, H. Malekpour, B. Alonso, A. Centeno, A. Zurutuza, A.I. Cocemasov, D.L. Nika, and A.A. Balandin: Adv. Funct. Mater., 25, (2015) 4664.
[30] J. Saranya, P. Saminathan, S.R. Ankireddy, M.R. Shaik, M. Khan, and B. Shaik: Biomedicines, 11, (2023) 531.
[31] R. Karthika, M. Govindasamy, S. Chen, T. Chena, J.V. Kumar, A. Elangovan, V. Muthuraj, and M. Yu: RSC Adv., 7, (2017) 25702.
[32] S. Panda, V. Marla, V.S. Aditya, and V.S. Sarma: Sustain. Energy Fuels, 5, (2021) 4414.
[33] C. Min, Z. He, H. Song, D. Liu, W. Jia, J. Qian, Y. Jin, and L. Guo: Appl. Sci., 9, (2019) 170.
[34] T. Liu, Y. Zhang, X. Yang, X. Hao, X. Liang, F. Liu, F. Liu, X. Yan, J. Ouyang, and G. Lu: Sens. Actuators B Chem., 276, (2018) 489.
[35] X. Nie, R. Zhang, Z. Tang, H. Wang, P. Deng, and Y. Tang: Microchem. J., 159, (2020) 105367.
[36] R. Suresh, V. Ponnuswamy, and R. Mariappan: Appl. Surf. Sci., 273, (2013) 457.
[37] E. Fazio, B. Gökce, A.D. Giacomo, M. Meneghetti, G. Compagnini, M. Tommasini, F. Waag, A. Lucotti, C.G. Zanchi, P.M. Ossi, M. Dell'Aglio, L. D'Urso, M. Condorelli, V. Scardaci, F. Biscaglia, L. Litti, M. Gobbo, G. Gallo, M. Santoro, S. Trusso, and F. Neri: Nanomaterials (Basel), 10, (2020) 2317.
[38] D. Zhang, B. Gökce, C. Notthoff, and S. Barcikowski: Sci. Rep., 5, (2015) 13661.
[39] T. Sakka, S. Iwanaga, Y.H. Ogata, A. Matsunawa, and T. Takemoto: J. Chem. Phys., 112, (2000) 8645.
[40] H. Wang, A.A. Pyatenko, K. Kawaguchi, X. Li, Z. Warkocka, and N. Koshizaki: Angew. Chem. Int. Edit., 122, (2010) 6505.
[41] A. Pyatenko, M. Yamaguchi, and M. Suzuki: J. Phys. Chem., 22, (2007) 111.
[42] M.P. Navas, R.K. Soni, N. Tarasenka, and N. Tarasenko: Appl. Surf. Sci., 414, (2017) 413.
[43] J.R. Jesus, R.J.S. Lima, K.O. Moura, J.G.S. Duque, and C.T. Meneses: Ceram. Int., 44, (2018) 3585.
[44] A. Kanitz, M.R. Kalus, E.L. Gurevich, A. Ostendorf, S. Barcikowski, and D. Amans: Plasma Sources Sci. Technol., 28, (2019) 103001.
[45] A. Shrivastava: "Introduction to Plastics Engineering" ed. by A. Shrivastav, (William Andrew Publishing, 2018) p. 17.
[46] V. Khoshkava and M. R. Kamal: Biomacromolecules, 14, (2013) 3155.
[47] A.M. Ali and S. Hasegawa: Thin Solid Films, 437, (2003) 68.
[48] M. Shi, Y. Kitamoto, M. Hara, and H. Wada: Appl. Phys. A, 128, (2022) 968.
[49] Y. Liu, J.S. Xue, T. Zheng, and J.R. Dahn: Carbon, 34, (1996) 193.
[50] R. Phillips, K. Jolley, Y. Zhou, and R. Smith: Carbon Trends, 5, (2021) 100124.

[51] R. Pasricha, S. Gupta, and A. K. Srivastava: Small, 5, (2009) 2253.
[52] M. Ashokkumar: Ultrasonics Sonochemistry, 18, (2011) 864.
[53] C. Zhao, Q. Wang, H. Zhang, S. Passerini, and X. Qian: ACS Appl. Mater. Interfaces, 8, (2016) 15661.
[54] P.V. Tuan, H.B. Tuong, V.T. Tan, L.H. Thu, N.D. Khoang, and T.N. Khiem: Opt. Mater., 123, (2022) 111916.

(Received: June 15, 2023, Accepted: November 12, 2023)